Computers and Chemical Engineering 178 (2023) 108400

Contents lists available at ScienceDirect

Computers and Chemical Engineering

journal homepage: www.elsevier.com/locate/cace

Computational fluid dynamics modeling of a discrete feed atomic layer deposition reactor: Application to reactor design and operation

Matthew Tom [a], Henrik Wang [a], Feiyang Ou [a], Sungil Yun [a], Gerassimos Orkoulas [c], Panagiotis D. Christofides [a,b,*]

[a] Department of Chemical and Biomolecular Engineering, University of California, Los Angeles, CA, 90095-1592, USA
[b] Department of Electrical and Computer Engineering, University of California, Los Angeles, CA 90095-1592, USA
[c] Department of Chemical Engineering, Widener University, Chester, PA 19013, USA

ARTICLE INFO

Keywords:
Computational fluid dynamics modeling
Semiconductor manufacturing processes
Area-selective atomic layer deposition
Reactor optimal design
Reactor optimal operation

ABSTRACT

Novel transistor fabrication methods such as area-selective atomic layer deposition (AS-ALD) are crucial to improving nanopatterning, which is essential for facilitating transistor stacking in semiconducting wafers. However, transistor surfaces are subjected to nonuniformities during the initial AS-ALD adsorption reactions that are attributed to steric hindrance effects. To minimize the role of steric hindrance generated by an oversaturation of reagent on the substrate surface, a discrete feed method is proposed for an ALD reactor configuration where reagent is introduced in short pulses through a perpendicular delivery system. An optimal reactor configuration is developed by modifying the inlet geometries of the reactor to ensure ideal fluid dynamics conditions (e.g., minimal vortices, radial flow distribution) are achieved. Detailed computational fluid dynamics simulations demonstrate the performance of the new reactor configuration and operational strategy.

1. Introduction

The last decade has seen a major series of progressions in the architectures of nanoscale devices. Various flaws that contribute to the degradation of semiconductor transistor performance have been addressed, including reducing current leakage and short-channel effects (Asenov et al., 2016; Huang, 2022) by implementing the gate-all-around design (Loubet et al., 2017), which is suitable for transistors with small feature sizes at the nanoscale. The densification of transistors in wafers, particularly through the miniaturization of transistor dimensions toward two-dimensional attributes and the conjoining of transistors through vertical or horizontal stacking (Schram et al., 2022) continue to align with the predictions of Moore's Law (Moore, 1998) while minimizing expenses, improving power efficiency, and enhancing computational performance (Wang et al., 2022). Consumers benefit from the increased performance of these nanoscale devices, which are being incorporated into a plethora of applications in smart system technologies, medical, gaming, computing, and telecommunications industries (Anitha et al., 2015; Petti et al., 2016) as pictured in Fig. 1. However, the fabrication of these nanoscale devices, which require stringent product requirements, is an ongoing challenge that is arguably associated with high inventory turnover, a measure of the demand against the supply of the product (Lee et al., 2017).

Recently, the demand for high-performance electronics in the United States has been increasing owing to a variety of factors, including increased application of artificial intelligence tools and broad implementation of smart manufacturing practices in industry (Handwerker, 2021). Future predictions speculate the potential for four-fold global semiconductor sales by 2030, which are exacerbated by the rising demand for high-performance computing and automation (Dziczek, 2022). However, the United States accounts for only 12% of the global production of semiconductor chips, which stokes fears of potential shortage for these chips in the United States as a result of limited production. In response to the limited availability of these semiconductors (Mohammad et al., 2022), the United States invested more funding toward research in 2022 to improve inefficient manufacturing practices with more productive and accurate procedures and develop advanced technologies that are intended to fabricate wafers more efficiently with highly conformal quality (Meng and Goodrich, 2021; Swanson, 2023). Efforts to achieve highly conformal film quality have proven successful in the last two decades with the emergence of new techniques such as atomic layer deposition (ALD) (George, 2010; Johnson et al., 2014), atomic layer etching (ALE) (Carver et al., 2015; Kanarik et al., 2015), and area-selective atomic layer deposition (AS-ALD) (Chen et al., 2005; Mackus et al., 2019; Andreoni and Yip, 2020). These cutting edge

* Corresponding author at: Department of Chemical and Biomolecular Engineering, University of California, Los Angeles, CA, 90095-1592, USA.
E-mail address: pdc@seas.ucla.edu (P.D. Christofides).

https://doi.org/10.1016/j.compchemeng.2023.108400
Received 3 August 2023; Received in revised form 27 August 2023; Accepted 28 August 2023
Available online 1 September 2023

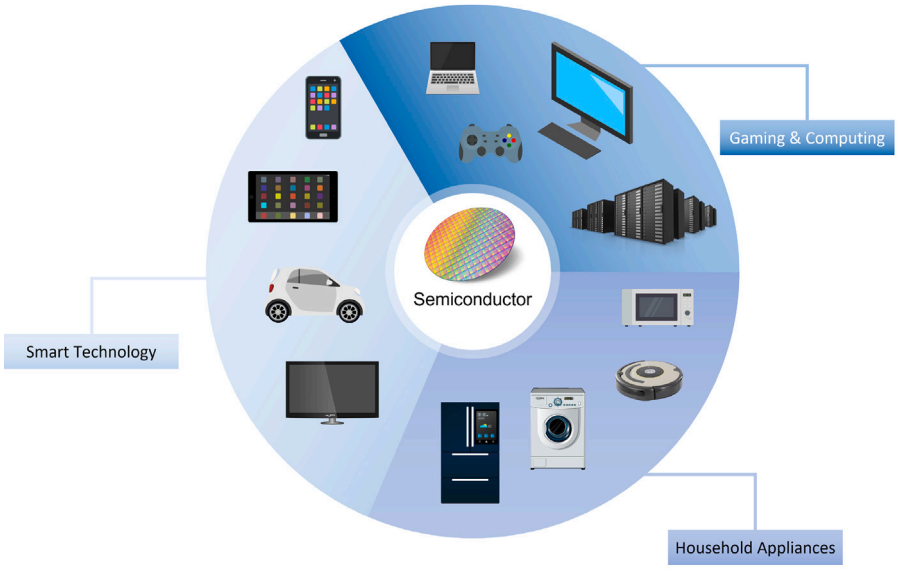

Fig. 1. Chart depicting the semiconductor usage in a diverse economy of electronic devices.

fabrication methods are conducted with countless reagents such as plasma, oxidative agents, and chemical inhibitors, or through high-temperature environments. Previously, bottom-up fabrication methods using atomic layer deposition, in which sequential cycles of surface modification and deposition steps are performed to produce transistors that are assembled on a wafer plane, were conducted in the semiconductor manufacturing industry (George, 2010). However, new research has been centered on preserving or enhancing surface uniformity to facilitate the self-alignment of transistors during the stacking process (Powell et al., 2000; Cao et al., 2020) using atomic layer etching as a post-processing, top-down, procedure following ALD (Faraz et al., 2015) or area-selective atomic layer deposition (AS-ALD), which does not require atomic layer etching steps. Recently, AS-ALD has been recognized as a pivotal process for achieving higher product yield with high film quality and greater control of localized nanopatterning through self-assembled monolayers (SAMs) (Lee and Bent, 2011).

In addition to the chemical mechanisms for semiconductor fabrication, the optimization of reactors and operating conditions are necessary for achieving greater product yield and film quality. Various reactor modeling proposals and patents have been developed, particularly batch (stationary) (Elers et al., 2006) and spatial (Poodt et al., 2012; De la Huerta et al., 2018) configurations as depicted in Fig. 2. Additionally, reactor models have been constructed with different approaches. Variations include the configuration of the reagent delivery system to the substrate through cross or perpendicular (overhead) flow distributions (Elers et al., 2006; Kimes et al., 2012) as shown in Fig. 3, continuous feed (Ritala and Leskelä, 2002; Muñoz-Rojas et al., 2019) or discrete feed (Lin et al., 2023) pulses, and fluid partitioning by using dividers such as showerheads (Lee et al., 2007) and inclined plates (George, 2010) as illustrated in Fig. 4, or substrate holders (Dahmen, 2003) to minimize reagent concentration gradients on the surface of the substrate. While the development of these reactors is a first step toward their integration to industrial applications, *in silico* modeling (Deng et al., 2016b) provides an effective approach to studying the behavior of the fluid dynamics for a variety of reactor models, particularly small reactor models, that will improve the process efficiency of the reactor and maximize reagent usage. For instance, spatial reactor models for AS-ALD and ALD perform poorly at attaining complete surface coverage due to the overdosage of reagent to the wafer surface, thereby risking the integrity of self-aligning transistors during this bottom-up fabrication procedure. In particular, this work will examine the fluid dynamics of a stationary-type reactor that employs a perpendicular feed mechanism with a showerhead distributor that will be used for an area-selective atomic layer deposition (AS-ALD) process.

Past works (Mameli et al., 2017; Merkx et al., 2020, 2022) have studied the effectiveness of integrating AS-ALD reaction mechanisms using small molecule inhibitors (SMIs) to reduce post-processing etching and lithography steps to improve the substrate film uniformity (Mackus et al., 2014). However, the aforementioned works require *in vitro* experiments, which are time-consuming, difficult to replicate in similar operating conditions, and challenging to quantitatively characterize with limited data. Thus, *in silico* modeling facilitates the procedures for gathering data more efficiently while also generating large data sets that align with the findings from experimental works. For instance, prior works (Yun et al., 2022b,c) have focused on multiscale modeling, an intricate simulation configuration that conjoins microscopic, mesoscopic, and macroscopic modeling (Maroudas, 2000; Christofides et al., 2009), of various reactor designs, stationary and spatial, using different reagent delivery systems (showerhead, plate, cross-flow, and perpendicular flow) for ALE processes. Most recently, Yun et al. (2023) conducted multiscale computational fluid dynamics (CFD) modeling to study the spatiotemporal behavior of reagent distribution in a spatial-type rotary reactor for an AS-ALD process. Several works have also examined the optimization of reactor design for spatial reactors for ALD processes (Pan et al., 2016; Cong et al., 2020; Pan, 2021) and the optimization of reactor operating conditions (Deng et al., 2016a,b) using CFD. Thus, *in silico* modeling presents an alternative approach for data collection and reactor performance evaluation, which enables the development of advanced technologies that are capable of producing highly conformal thin films by studying the spatiotemporal behaviors of species pressure, temperature, and velocity profiles to further optimize reactor and process design. Particularly, this work will examine the role of the reactor geometry on the fluid dynamics on the substrate surface that can be employed for industrial applications for semiconductor manufacturing.

Motivated by the above considerations, this work will employ computational fluid dynamics (CFD) modeling to study the behavior of the fluid dynamics within the discrete feed reactor model proposed by Lin et al. (2023) for an AS-ALD process characterized by Mameli et al. (2017). One caveat of the AS-ALD process is that steric hindrance plays an important role in the process. Steric hindrance is caused by bulky molecular species such as bis-diethylaminosilane (BDEAS), and it can

Fig. 2. (a) Stationary and (b) spatial, sheet-to-sheet, reactor configurations for thin-layer deposition and etching processes.

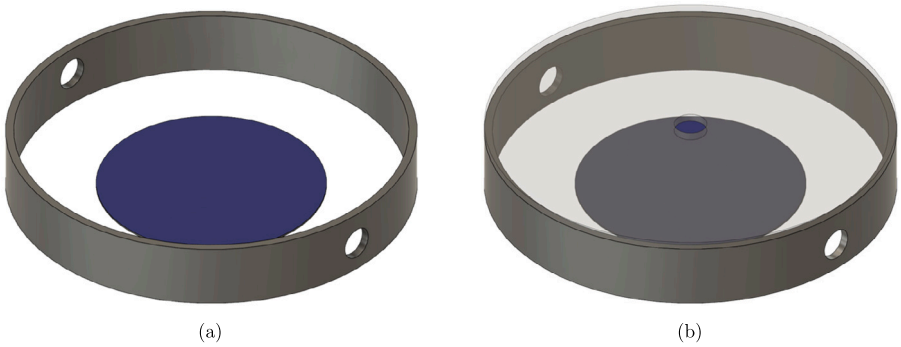

Fig. 3. (a) Cross-flow orientation where feed is introduced parallel to the substrate surface, and (b) perpendicular flow orientation where feed is introduced above the substrate surface for thin-layer deposition and etching processes.

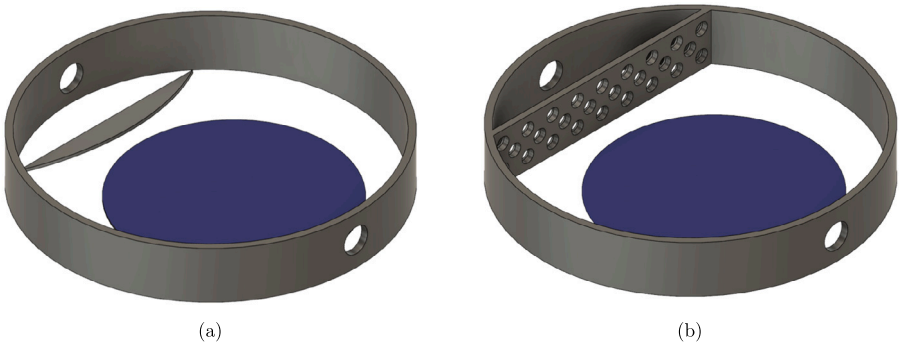

Fig. 4. (a) Inclined plate and (b) showerhead distributors to control reagent flow uniformity for thin-layer deposition and etching processes.

introduce surface film deposition nonuniformities and cause incomplete surface coverage due to an excess of molecular interactions when the substrate is exposed to an abundance of reagents (Merkx et al., 2020; Li et al., 2022), which is exemplified in Fig. 5. Prior work (Yun et al., 2022a) studied these molecular interactions using a mesoscopic modeling simulation that is employed with a kinetic Monte Carlo (kMC) algorithm to stochastically simulate the adsorption reactions and the orientation of adsorbates on the substrate surface. The previous works (Yun et al., 2023; Tom et al., 2023) performed multiscale CFD modeling for an AS-ALD process with a silica/alumina substrate for the optimization of an advanced spatial, rotary reactor configuration. However, these works did not account for reactor optimization for mitigating the screening effects induced by steric repulsions, which lead to incomplete surface coverage (i.e., lower observed deposition rates) and ultimately nonuniform thin film surfaces. This work will perform computational optimization of an AS-ALD stationary reactor using a discrete feed method (DFM) to control the fluid dynamics of the reagents on the surface of the substrate. Several factors including the evacuation of gases and temporal progression of surface pressure will be discussed to determine saturation pressures that will be beneficial for discrete feed modeling in future multiscale modeling work for the same reactor geometry. For instance, Xiong et al. (2021) studied the fluid velocity distribution of ALD processes on alumina through CFD modeling and the effect of precursor overdosage on homogeneous flow. Likewise, Chen et al. (2023) examined the role of precursor flow rate and residence time on the flow distribution. The ideal reactor has been optimized to have the following characteristics from a physical and computational perspective:

- Wafer surface saturation to initiate chemical adsorption (Park et al., 2011).
- Minimal entrainment of gaseous species (i.e., small residence time of gases to reduce steric effects).
- Reactor design that is appropriately meshed to meet simulation standards (ANSYS, 2022a) while yielding realistic simulation time demands.

Additionally, the present work examines the fluid dynamics, particularly the uniformity of the reagent distribution, which is crucial for

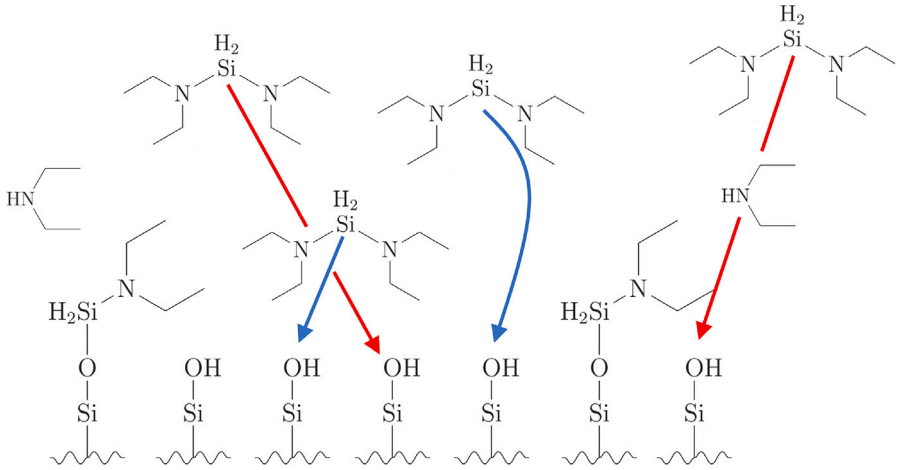

Fig. 5. Illustration of the steric hindrance screening effect caused by excess reagent or overproduction of byproduct such as diethylamine (DEA), blocking precursors such as bis-diethylaminosilane (BDEAS) from adsorbing to the substrate surface composed of SiO_2. Red arrows indicate screening effects from DEA and excess BDEAS while blue arrows have a probable adsorption path.

achieving high film uniformity. Likewise, this work aims to determine the saturation time, which is when the wafer is fully exposed to the reagents, and purging times, which is when all reagents are completely removed from the reactor, to determine appropriate operating conditions for future multiscale modeling research on the discrete feed mechanism for this reactor design, and to provide an applicable reactor configuration for potential integration into industrial applications. The utilization of the DFM and the optimization of reactor models to counter the effects of steric hindrance will enable the development of large-scale, advanced reactors for ALD and AS-ALD processes by examining the effect of the inlet geometry on the uniform distribution of reagent along the substrate surface, which is a vital condition to enable the production of highly conformal thin film surfaces.

This manuscript will be organized in several sections. Section 2 will examine the development of the CFD simulation through reactor design and optimization, meshing, and CFD modeling construction through Ansys fluids products, and Section 3 will evaluate the fluid dynamics of the reactor model, and discuss procedures intended to maintain film uniformity and maximize the deposition rate per cycle.

2. Computational fluid dynamics modeling framework

This work proposes a computational fluid dynamics (CFD) model for a reactor configuration that is developed through a framework of various software tools (to be discussed below) to replicate the conditions of AS-ALD for a discrete feed method (DFM) approach. The reactor that this paper discusses is modeled loosely using a previously developed design (Lin et al., 2023) that is constructed through computer aided design (CAD) software. Consequently, the reactor geometry is discretized into a mesh that conforms to software quality criteria (ANSYS, 2022a) while simultaneously reducing the computational strain on the simulation. CFD is later utilized to model the various reactor configurations that are characterized by different reagent delivery systems to study the spatiotemporal behavior of the gases, particularly the development of laminar flow, the evacuation of gases, the formation of vortices, and the distribution of gases. Such conditions will ensure that the reactor is constructed and optimized to ensure that the resulting flow behavior will achieve film uniformity and purge byproducts sufficiently to limit the effects of steric hindrance. This section discusses the procedural steps and assumptions conducted for the construction of the reactor through CAD software, Ansys DesignModeler, and meshing and CFD simulation through Ansys multiphysics software, Fluent.

2.1. The impact of steric hindrance

Steric shielding is caused by the bulkiness of molecular species expanding beyond molecular distances between substrate atoms (Simon and Aarik, 1997; Puurunen, 2005). This repulsion effect is also influenced by the formation of byproducts that hinder the adsorbates and small reactive site distances that facilitate the adsorption of bulky adsorbates. Thus, the self-limiting behavior of AS-ALD, such that monolayers of surface material are deposited with each cycle, is not observed due to the effects of steric hindrance (Xu et al., 2022), and limits the reaction pathway. Following the rate-limited adsorptions, the surface of the wafer will experience an oversaturation of reagent, which will be exhausted and wasteful for the process. To leverage the screening effects induced by the bulky adsorbates, small molecule inhibitors (SMIs) have been integrated into AS-ALD processes (Yarbrough et al., 2021, 2022), where the steric behavior of an SMI was simulated in prior work through kinetic Monte Carlo (kMC) simulation, which uses a stochastic procedure to replicate the conversion of active surface sites in the atomic scale and atomistic methods that employ *ab initio* quantum mechanics simulations to evaluate kinetic parameters (Yun et al., 2022a). Several works have proposed discrete reagent delivery methods that occur in short pulses with sequential purging pulses to reduce the generation of byproduct species, thereby minimizing the intermolecular collisions with adsorbates (Wang et al., 2019; Lee et al., 2023). For instance, Muneshwar and Cadien (2016) proposed a pulsed feed method using a numerical study by introducing a steric factor to replicate the rate-limiting behavior of adsorption reactions. Park et al. (2011) conducted a discrete feed method for atomic layer deposition of HfO thin films to mitigate the screening effects by suppressing reagent overdosage, and observed higher growth film rate and improved electrical properties of the film. Motivated by the prior works, this work aims to consider the role of steric hindrance in an AS-ALD process and to adopt reactor configurations that are appropriate for minimizing the role of screening effects for adsorption reactions.

2.2. Computational fluid dynamics modeling equations

The spatiotemporal behavior of the fluid transport is captured by numerically solving the mass, momentum, and energy transport equations, which are the fundamental equations that characterize the motion of the fluids in the reactor. The mass and momentum balance equations are defined by the following expressions, respectively:

$$\frac{\partial \rho}{\partial t} + \nabla \cdot \left(\rho \vec{v}\right) = S_m \tag{1}$$

Table 1
Dimensions for the reactor configurations.

Reactor dimension	Value
Plate diameter	290 mm
Ring inlet outer diameter	170 mm
Ring inlet inner diameter	130 mm
Round inlet diameter	20 mm
Round outlet diameter	4 mm
Showerhead diameter	250 mm
Showerhead pores diameter	10 mm
Showerhead thickness	0.5 mm
Showerhead-wafer gap distance	5 mm
Inlet-showerhead gap distance	3 mm
Wall sector angle	40°

$$\frac{\partial\left(\rho\vec{v}\right)}{\partial t}+\nabla\cdot\left(\rho\vec{v}\vec{v}\right)=-\nabla P+\nabla\cdot\left(\bar{\bar{\tau}}\right)+\rho\vec{g}+\vec{F} \tag{2}$$

where ρ is defined to be the density of the fluid mixture, $\vec{v}$ represents the velocity of the fluid mixture, S_m is the mass transfer source rate, P is the static pressure of the system, $\bar{\bar{\tau}}$ denotes the symmetric, second-order rank, stress tensor term, $\rho\vec{g}$ is the gravitational body force exerted by the fluid mixture, and $\vec{F}$ reflects the external body force on the fluid mixture.

Additionally, the energy conservation of the system is expressed by the following equation:

$$\frac{\partial}{\partial t}\left(\rho E\right)+\nabla\left(\vec{v}\left(\rho E+P\right)\right)=-\nabla\left(\Sigma h_j\vec{J}_j\right)+S_h \tag{3}$$

where E represents the internal energy of the system, h_j expresses the sensible enthalpy of fluid species j, S_h denotes the heat transfer source rate, and $\vec{J}_j$ describes the mass diffusion flux rate of fluid species. The transport equations will be simplified by making assumptions to the reactor design that are elucidated in Section 2.5.

2.3. Reactor designs

With the laminar viscous model defined, various three-dimensional (3D) reactor configurations are constructed by modifying the geometry of the gas delivery system to the substrate (e.g., the showerhead and shape of the inlet). The inlet to the reactor is positioned above the showerhead divider to allow the reagent to flow perpendicular to the surface of the substrate, and the reactor outlets are oriented along the lateral sides of the reactor to allow the gases to evacuate in a cross-flow manner. The reactor geometry is constructed using Ansys DesignModeler using a reactor model that employs the discrete feed method (DFM) with a perpendicular flow orientation through a showerhead plate (Lin et al., 2023). The reactor has a cylindrical body that is 300 mm in diameter and 8 mm in height, where the lateral region contains an inlet and outlet for the substrate and for the evacuation of gases, which is illustrated in Fig. 6. The gap distance between the inlet (4) to the showerhead (5) is 3 mm, where the showerhead is composed of pores that are 10 mm in diameter, and the gap distance between the showerhead and the substrate is 5 mm. The outflows (3) have a diameter of 4 mm, and the wall is constructed with a sector angle of 40°. Additionally, the wafer (1) is modeled as a thin, 250-mm diameter surface which rests on a plate (2), which allows the wafer to enter and exit the reaction zone (6) by way of a rotating conveyor belt that is similar to the rotary reactor modeled in a prior work (Yun et al., 2023). A summary of the reactor configuration dimensions are provided in Table 1.

The reactor configuration design will be analyzed by changing the geometry of the modeled inlet. Various inlet geometries include a single round inlet (Case 1), multiple round inlets (Case 2), a ring-shaped inlet (Case 3), and a combined ring-shaped and circular inlet (Case 4), which are all depicted in Fig. 7. The modification of the inlet geometries serves to provide a crucial understanding of their effect on the uniformity of the reagent distribution along the radial direction of the substrate. Such geometries also aim to prevent an excess of reagent delivery by placing the showerhead plate to limit the amount of reagent exposure, thereby reducing potential steric shielding caused by molecular collisions between byproducts and unreacted reagent.

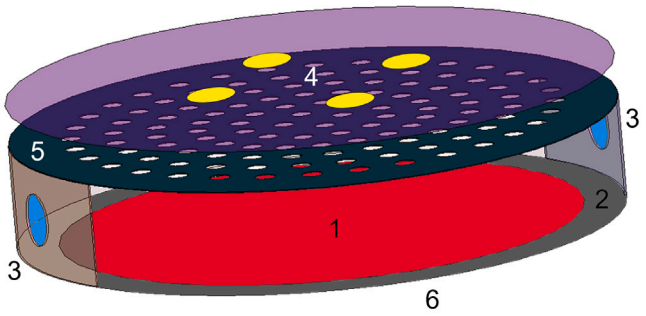

Fig. 6. Schematic of the proposed reactor constructed using CAD modeling software, Ansys DesignModeler, containing a (1) substrate (in red), (2) substrate holder or bottom plate (in gray), (3) outflows (in blue), (4) inlets (in yellow), (5) showerhead distributor (in teal), and (6) wafer inlet and exit from the reactor chamber, which also serves as an outlet for gases.

2.4. Reactor meshing

To generate spatiotemporal data for the reactor, a finite element approach is integrated into the work by discretizing the reactor geometry into cells through a meshing procedure. The Meshing Mode of Ansys Fluent contains several functions that optimize the efficiency and accuracy of the computations depending on the fineness or size of the mesh while defining the geometry of the cells and the resolution of the mesh. A nonuniform mesh resolution is fundamental to the meshing procedures, which densifies discretized elements in boundary layer zones and disperses cells with increasing distance from the boundary layers. Additionally, several features are available to improve the quality of the mesh to conform to recommended mesh quality criteria by the Ansys guidelines (ANSYS, 2022a) to ensure that simulation accuracy and efficiency are appropriately balanced. Such mesh quality parameters include the minimum orthogonality, the skewness, and the aspect ratio as summarized in Table 2, which are important features that are intended to preserve the computational accuracy and efficiency of the simulation.

The minimum orthogonality is a parameter that measures the quality (accuracy and stability) of the mesh. This quality indicator is calculated by finding the minimum value of the normalized dot product of an area vector from a face $\vec{A}_i$ for a cell i and a vector from the centroid of the cell, i, to the face, $\vec{f}_i$, and the normalized dot product of area vectors of a face $\vec{A}_i$ for a cell i and a vector from the centroid of a cell i and the centroid of an adjacent cell that shares the same face $\vec{c}_i$ for all cells, N, in the mesh. An ideal mesh would have a minimum orthogonality of unity.

$$\text{Orthogonality}=\min\left(\frac{\vec{A}_i\cdot\vec{f}_i}{\left|\vec{A}_i\right|\left|\vec{f}_i\right|},\frac{\vec{A}_i\cdot\vec{c}_i}{\left|\vec{A}_i\right|\left|\vec{c}_i\right|}\right)\quad\forall\, i\in\{1,2,\ldots,N\} \tag{4}$$

The minimum orthogonality is selected for all cells and is expressed in Table 2.

The skewness is a measure of the rigidity of a cell, i, from its equilateral counterpart, which is defined as the ratio between the difference of the equilateral cell volume, $V_{eq,i}$ and cell volume $V_{c,i}$ to the equilateral cell volume, as follows:

$$\text{Skewness}=\frac{\left|V_{eq,i}-V_{c,i}\right|}{V_{eq,i}}\quad\forall i\in\{1,2,\ldots,N\} \tag{5}$$

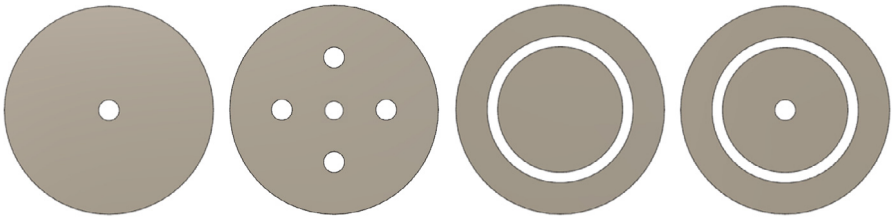

Fig. 7. Inlet geometries composed of the (a) single round inlet, (b) multi-round inlet, (c) ring inlet, and (d) combined round and ring inlet, which are examined for their performance in the reactor model.

Table 2
The mesh quality for various reactor configurations in comparison to mesh quality standards provided by Ansys Fluent.

Quality indicator	Orthogonality	Skewness	Aspect ratio	Number of cells
Criteria range	0.001 ~ 1[a]	0[a] ~ 0.95	1[a] ~ 8	N/A
Case 1	0.140	0.443	3.022	1,181,523
Case 2	0.105	0.451	3.040	1,149,495
Case 3	0.097	0.448	3.028	1,171,125
Case 4	0.103	0.449	3.029	1,178,849

[a] Desired value for ideal mesh quality.

The averaged value of the skewness of all cells, N, in the mesh is expressed in Table 2, and a skewness close to 0 is desirable.

Lastly, the aspect ratio is a quality parameter that characterizes the stretching of a cell i by comparing the maximum and minimum values of the distance between the centroid of the cell to the centroid of a face in the cell, $d_{f,i}$ or the distance between the centroid of the cell to a node in the cell, $d_{n,i}$.

$$\text{Aspect Ratio} = \frac{\max\left(d_{f,i}, d_{n,i}\right)}{\min\left(d_{f,i}, d_{n,i}\right)} \quad \forall i \in \{1, 2, \ldots, N\} \tag{6}$$

The averaged aspect ratio for all cells is evaluated and expressed in Table 2.

Several user-defined parameters of the mesh are defined to reduce the number of cells while maintaining a robust quality, which includes the cell growth rate on the surface and inside the reactor volume (1.5) and the minimum and maximum cell lengths (0.36 mm and 7.8 mm, respectively). The meshing software also employs algorithms intended to improve the organization, structure, and quality of the mesh by removing obsolete cells and restructuring irregular cell geometry in essential boundary layer zones. Additionally, tetrahedral volume cells and triangular surface cells are utilized for the three-dimensional (3D) reactor mesh. The quality of the meshes for each of the reactor configurations are shown in Table 2 and indicate that all meshes are within the appropriate tolerances for mesh quality indicators; thus, simulations are conducted with high computational accuracy and efficiency.

2.5. Simulation development and parameters

By applying the mass and momentum conservation equations described by Eqs. (1) and (2), the spatiotemporal behavior of the delivery system of reagent to the substrate surface is studied and then optimized so that the inlet geometry and showerhead will achieve substantial exposure uniformity for small pulse times. Additionally, the design of the reactor outflow must minimize the residence time of the byproducts and excess reagents within the reaction zone, minimize the effect of steric hindrance on surface nonuniformities, and also maximize the amount of deposited material within the deposition cycle. Therefore, the ideal residence time for all species is low as a consequence of the combined pressure force induced by the outflow vacuum pressure and the tendency for gases to migrate toward regions of lower concentration. It is also notable that this work simplifies Eq. (1) by neglecting the mass species source term, S_m, due to this work focusing specifically on the fluid dynamics of the system to optimize the species delivery and purging systems for the reactor. Therefore, reactions and chemical kinetics are not considered for this aspect of the work.

The reagent delivery system of the reactor must overcome the mass suction forces generated by the vacuum pressure outflow parameters that cause the gases to migrate radially outward from the center of the wafer, while simultaneously reducing the residence time of the gases in the reactor. To lessen the potential formation of fluid vortices and eddies, the reagents and carrier gases are delivered in laminar conditions, which also minimizes reagent usage, minimizes reactor size, and simplifies the computational complexity of the model (Ponraj et al., 2013). Thus, the reagent delivery to the wafer surface is influenced by the gravitational force and mass diffusion due to the assumptions that the external body and viscous forces within $\overline{F}$ in Eq. (2) are negligible when the laminar model in Ansys Fluent is defined in the CFD simulation (ANSYS, 2022b). With the laminar model specified, the diffusion flux rate for gas species j, $\overline{J}_j$ presented in Eq. (3) is defined by the following fundamental expression that is referred to as Fick's Law:

$$\overline{J}_j = -\rho D_{j,m} \nabla y_j - D_{T,j} \frac{\nabla T}{T} \tag{7}$$

where $D_{j,m}$ denotes the mass diffusion coefficient for species, j, y_j represents the mole fraction for species j, and $D_{T,j}$ describes the thermal or Soret diffusion coefficient. The CFD simulation also operates under isothermal conditions, assuming that the reactor has a suitable temperature control system; therefore, in Eq. (7), the mass diffusion flux is dependent only on concentration gradients within the fluid mixture.

The fluid flow pattern may be classified by the Reynolds number, Re, which describes flow as being laminar, transient, or turbulent and is defined as follows:

$$Re = \frac{\rho \vec{v} D}{\mu}$$

By assuming that the dynamic viscosity (μ), density (ρ), and mass flow rate of the fluid for each inlet configuration (hence the velocity, $\vec{v}$ of the fluid exiting the inlet is constant) in Cases 1 through 4 are constant, the Reynolds number is dependent on the characteristic length, D. The characteristic lengths for the round inlet and ring-shaped inlet depend on the ratio of the surface area, A_{inlet}, of the inlet and the wetted perimeter, P_{inlet} of the inlet that can be calculated as follows:

$$D_{ring} = \frac{4A_{ring}}{P_{ring}} = \frac{\pi d_o^2 - \pi d_i^2}{\pi d_o + \pi d_i} = d_o - d_i \tag{8}$$

$$D_{round} = \frac{4A_{round}}{P_{round}} = \frac{\pi d^2}{\pi d} = d \tag{9}$$

The characteristic length of concentric circles described by the ring inlet in Eq. (8) depends on the inner and outer diameters (d_o and d_i, respectively), while the characteristic length of a circle described by the round inlet in Eq. (9) depends on the diameter, d, of the inlet.

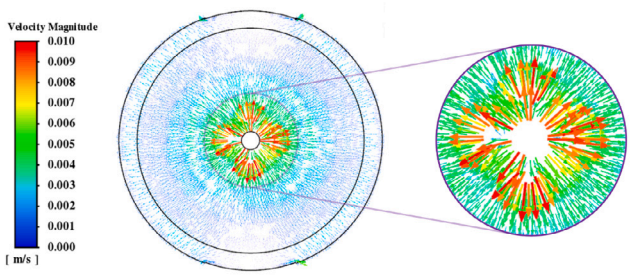

(a) Case 1

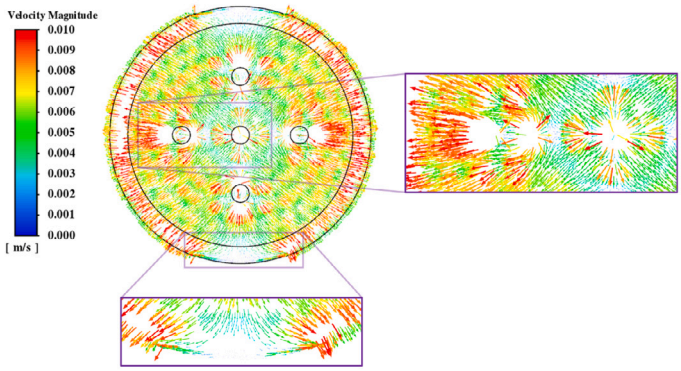

(b) Case 2

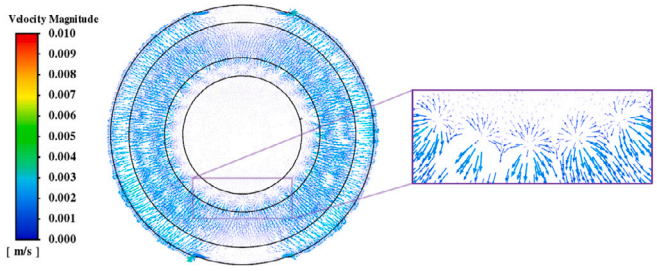

(c) Case 3

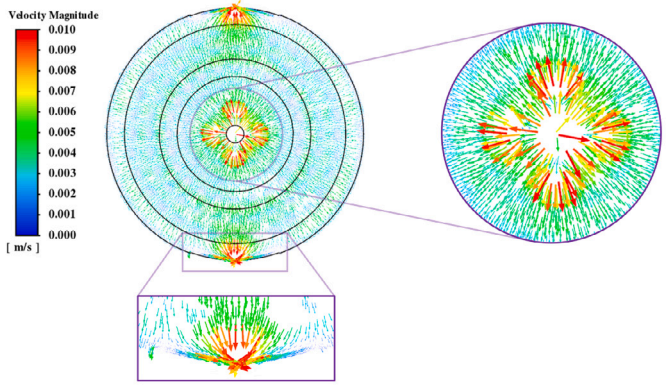

(d) Case 4

Fig. 8. Velocity magnitude fields for the four reactor configurations at process times of 3 s. One-direction radial flow from the center to the outer regions of the reactor wall ensures minimal reagent intermixing that disrupts uniform flow behavior. This disturbed flow is exemplified by Case 2 while Cases 1 and 4 produce a more homogeneous flow.

Several user specifications are designated within the simulation to replicate industrial processes, including the mass inflow and outflow rates, temperatures, and pressures, as well as simulation parameters intended to carry out the numerical computations through finite element discretization methods and numerical solver approaches. For instance, the mass inflow and outflow boundary conditions are defined to the reactor model. Mass inflow rates for an arbitrarily chosen gaseous species are defined to have constant flow rates of 2.50×10^{-5} kg/s and constant mole fractions of 0.5. For this work, oxygen gas, O_2 is defined to the CFD model with material (e.g., density, viscosity, and thermal conductivity) and thermophysical property data (e.g., standard enthalpy, entropy, and heat capacity) selected from the Ansys Chemkin database. Outflow boundary conditions are specified to ensure that there is no accumulation of gas within the reactor and to prevent

Table 3
Parameters specified to the CFD model and solver.

Parameter	Value
Operating temperature	523 K
Operating pressure	101.3 kPa
Gas mass flow rate	2.50×10^{-5} kg/s
Gas mole fraction	0.50
Time step size	0.001 s
Maximum iterations per time step	200

backflow, such that the inflow gas flow rate would be equivalent to the outflow gas flow rate. The reactor operating temperature and pressure are defined to be 523 K and 101.3 kPa, respectively. A summary of all parameters defined to the model are provided in Table 3. The simulation will be conducted using a pressure-based coupled solver method that optimizes the computation speed by simultaneously solving the transport equations at the expense of requiring more random access memory (RAM) (ANSYS, 2022a). Additionally, the central processing unit (CPU), which consists of compute cores, has a substantial role in the parallel-computing environment that enables mesh partitioning for simultaneous computing of the CFD simulation. A fixed time step size of 0.001 s is selected for a first-order implicit numerical solver method to numerically solve the transient CFD process model, which satisfies the recommendations by the software for the global Courant number. Simulations are performed through a Linux computer cluster system comprising of two nodes with 36 and 48 computational cores and 384 GB and 512 GB of RAM, respectively, and averaging 6 to 8 h of simulation time to run 4 s of process time.

3. Simulation results and discussion

The computational fluid dynamics (CFD) simulation is performed to determine the role of the inlet configurations on the flow uniformity and understand what conditions will minimize the effects of steric hindrance that are caused by an oversaturation of reagents and byproducts in the vicinity of the substrate surface. To dilute this screening effect, the reagent delivery system limits the amount of exposure that the wafer has at any given time, thereby limiting the rate of reaction, particularly for the initial adsorption steps for the AS-ALD process. Thus, the flow profiles for each of the reactor models, particularly the velocity fields and pathlines illustrated in Figs. 8 and 9, respectively, and the mass transfer behavior presented in Fig. 10, provide a valuable depiction of the movement of gases on the substrate surface.

The velocity magnitude fields and pathlines provide an understanding of the dispersion of flow in the radial direction, as well as locations for fluid vortex and eddy formation. Fig. 8(a), for example, presents a homogeneous distribution of flow for the singular and round-shaped inlet reactor configuration, Case 1, without the formation of vortices or flow perturbations shown in Fig. 9(a). However, the velocity field for Case 1 indicates that all fluid movement is concentrated on the central region of the wafer, thereby extending the time to achieve complete saturation of the wafer surface, which is supported by the mole fraction contours for Case 1 in Fig. 10(a). The oversaturation of reagent to the substrate in a localized region increases repulsions between adsorbates and unexhausted reagent due to the increase in desorption reactions, which dominate over adsorption reactions as the coverage approaches unity (Holmqvist et al., 2012). Such results demonstrate that despite the small distance between the showerhead and inlets, the showerhead performs poorly at distributing the reagent due to the gravitational and body forces overcoming the effects of the vacuum forces at the outlet. Consequently, the reagent is unable to diffuse to the outer regions of the substrate in the initial stages of the delivery, which impacts the homogeneity of deposition. Thus, additional geometries, Cases 2 through 4, were created to improve the radial distribution of reagent, thus reducing the potential for large concentration gradients, which contribute to poor surface uniformity and steric repulsions.

The inclusion of multiple, round-shaped inlets for reactor model Case 2 was designed to improve the dispersion of the gases, which is illustrated by the vector fields in Fig. 8(b); however, there is an increasing likelihood for steric repulsions due to the opposing interactions between the inlet ports and flow field non-smoothness. The overconcentration of reagent resulted in disruptive flow behavior caused by increased convection from the combined gravitational forces and the perpendicular flow configuration. The inhomogeneous fluid flow is representative of the observations made by Xiong et al. (2021), who concluded that increased reagent pressure acts as a disturbance to the flow field, and leads to nonuniform deposition growth. Thus, the interactions worsened the radial distribution of reagent, which is pictured in Fig. 10(b) and generates highly concentrated regions that appear to increase the possibility of screening effects observed by the mole fraction contours of Case 1 in Fig. 10(a). Thus, a ring-shaped inlet configuration in reactor Case 3 was developed to improve the uniformity of the flow in the radial direction. Although the flow field presented in Figs. 8(c) and 9(c) indicates greater flow migration in the radial direction, the vacuum pressure of the outlets prevented further gas diffusion into the central regions of the wafer, which is depicted in Fig. 10(c), and limited the potential to achieve complete surface coverage of the wafer. To facilitate the distribution of gases toward the center of the wafer, an additional round-shaped inlet and ring-shaped inlet was positioned in the center of the inlet plate, which resulted in a more uniform movement of reagent in the radial direction by minimizing the gas interactions between both inlet configuration, which is presented in Figs. 8(d) and 9(d), and improved the distribution of reagent in the radial direction of the wafer in Fig. 10(d).

Conversely, Reynolds number plots produced in Fig. 11 illustrate that the fluid flow in all reactor models are laminar. However, the development of non-smooth flow profiles is influenced by the inlet geometry, which increased the potential for screening effects. The localization of reagent in the central region of the wafer led to the nonuniform flow distribution for reactor configuration Case 1, which is illustrated in Fig. 11(a). Likewise, Case 2 demonstrates that an overdosage of reagent through a multiple inlet configuration increases the potential for gas entrainment observed by Mousa et al. (2015) and eventual steric hindrance that restricts maximum deposition of substrate material in monolayers shown in Fig. 11(b). The observed increase in Reynolds number is caused by the increase in characteristic lengths produced by round-shaped inlet geometry in Eq. (9), which results in an increase in Reynolds number with added round inlets. As a result, a small number of inlets should be adopted into the inlet geometry to minimize flow non-smoothness. The appearance of turbulence in Case 4, which is illustrated in Fig. 11(d), is caused by the mixing of the reagents from both inlets, which may produce steric effects due to the pressure difference induced by the vacuum outlets across the wafer surface. The eventual pressure gradient causes variations in velocity in the radial direction of the wafer, which effectuated Reynolds number fluctuations. In contrast, the ring-shaped inlet in Case 3, visualized in Fig. 11(c), mitigates turbulent flow due to the symmetry of the inlet and the effective removal of reagent by the vacuum pressure. The observation is supported by the characteristic length for ring-shaped inlet geometry in Eq. (8), which reduces the Reynolds number for larger surface area. However, the central region of the wafer is unexposed to reagent as a consequence of this strong pressure difference between the inlet and outlet pressures, which limits reagent migration to the center of the wafer. Hence, further optimization of operating conditions, particularly the inlet flow rates, are needed for future study into the optimization of the AS-ALD process as a whole. From the aforementioned results, the inlet geometry of the AS-ALD reactor has a profound effect on the distribution of the flow, and on the quality of substrate. Furthermore, advanced technologies are able to employ inlet geometries that are structured with characteristic lengths that are capable of minimizing the Reynolds number and controlling the fluid dynamics on the substrate surface. A summary of results is provided

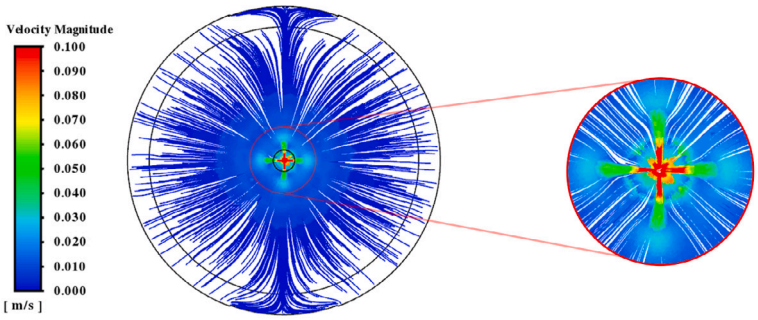

(a) Case 1

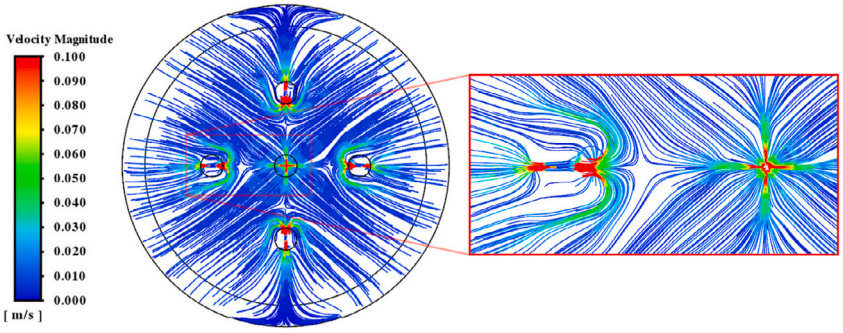

(b) Case 2

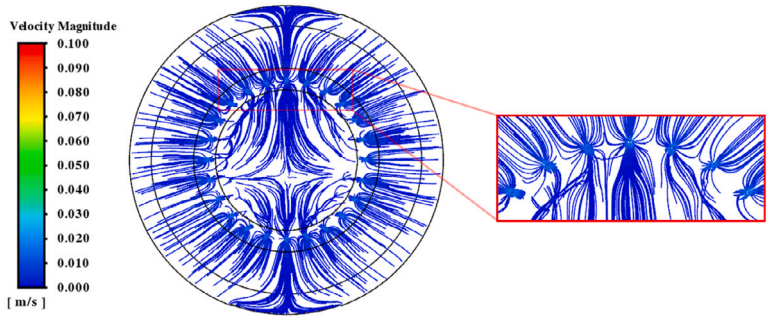

(c) Case 3

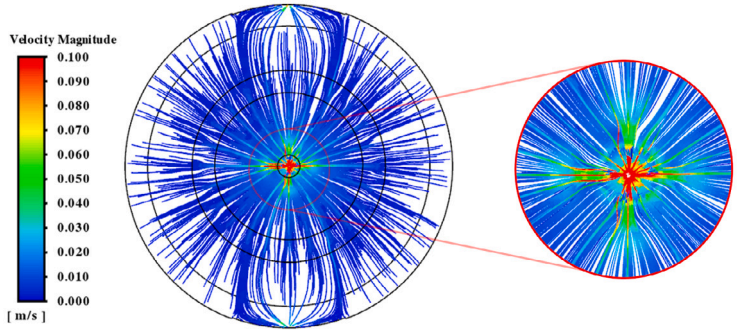

(d) Case 4

Fig. 9. Velocity magnitude pathlines for the four reactor configurations at process times of 3 s. The pathlines demonstrate the directionality of flow to ensure effective purging and minimal flow disruption is observed is Cases 1 and 4, while pathlines for Cases 3 and 4 indicate that backflow is possible.

Table 4
Comparison of reactor configurations based on criteria.

Reactor	Radial flow	Uniform distribution	Effective purging	Complete coverage
Case 1	✓	✓		
Case 2				
Case 3	✓	✓	✓	
Case 4	✓	✓	✓	✓

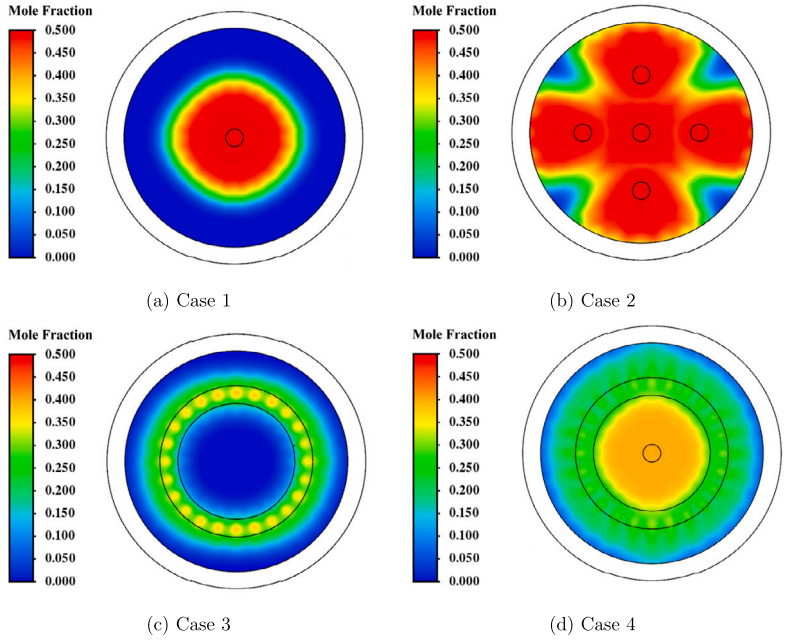

Fig. 10. Mole fractions of the gaseous species on the wafer surface for the four reactor configurations at process times of 3 s, which illustrate the dispersion of gases in the radial direction as well as complete surface exposure to gases. The contours for Case 4 are indicative of the aforementioned characteristics for radial fluid flow and complete surface exposure.

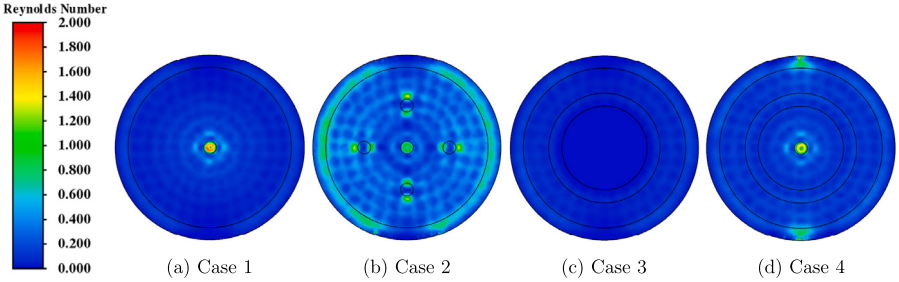

Fig. 11. Reynolds number contours of the substrate surface and bottom plate for all reactor configurations at process times of 3 s to discuss flow perturbations. Case 3 indicates that laminar flow is uniform throughout the reactor, suggesting that ring-shaped inlet geometry leads to laminar flow, and is supported by the characteristic length computation in Eq. (8).

in Table 4 to illustrate the effectiveness of inlet geometry design on radial flow, gas distribution, purging, and coverage completion within 3 s of process time.

In addition to the distribution of flow, the removal of gases from the reactor have an important role in minimizing the steric collisions between molecules during the initial adsorption phase. For each reactor model, four outlet ports were generated to prevent backflow of gases into the reaction zone. The velocity pathlines presented in Fig. 9 illustrate that all four reactor models effectively purge materials from the reaction zone. Particularly, Case 4 was studied to determine the time to achieve reagent exposure on all surfaces of the wafer and the time to effectively purge all material through a cut-in purging step. Results presented in Fig. 12 reveal that 3.8 s of reagent feeding is needed to achieve a saturation of the wafer surface, while 7.0 s of purging by feeding pure inert species was needed to evacuate all gas species from the reaction chamber after reagent surface saturation was observed. Arguably, the reagent dosage times are lower than that from Chen et al. (2023), who determined that longer dosage times are needed to achieve optimal growth rates. However, this work demonstrated the 7.0 s of purging time is analogous to the recommendations by Chen et al. (2023) of 7.0 s to 10.0 s. From an economics perspective, the Case 4 reactor configuration demonstrated that minimal reagent loss is observable with the spatially homogeneous distribution of reagent and the reduction in concentration to limit surface adsorption kinetics for preventing steric hindrance generated by screening effects. Thus, the reactor model illustrates that discontinuous feeding of reagent provides sufficient surface exposure within processing times analogous to spatial reactor configurations studied by Yun et al. (2022b, 2023). A further use of the modeling framework developed in this work would be to generate reactor variable profiles for a variety of operating conditions that can be used to augment experimental data and then use the overall data set to implement data-driven subspace identification for batch processes (Rashid and Mhaskar, 2023; Chandrasekar et al., 2023) to model and improve thin film (product) quality at the end of the batch.

4. Conclusions

With the rise of high-performance electronics, novel fabrication methods including area-selective atomic layer deposition (AS-ALD) are needed to improve the quality and production rate of semiconducting wafers that require stringent product specifications. The role of reactor configurations, particularly their inlet gas delivery systems, are of increasing interest to maintain wafer surface uniformity and coverage to improve nanopatterning and self-alignment for bottom-up fabrication of transistors. This work examined the impact of a new gas delivery system that employs a showerhead distributor, a perpendicular flow inlet,

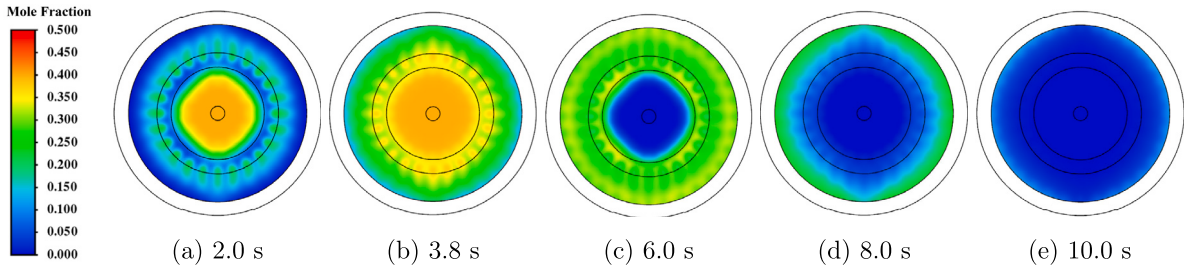

Fig. 12. Gas mole fraction on the substrate surface at various processing times for the Case 4 reactor geometry. Complete coverage is observed within 3.8 s of process time and takes 6.2 s or process time to achieve complete purging of reagents on the surface.

and cross-flow inlets on the distribution. Additionally, the removal of gaseous species from a reactor chamber to minimize steric hindrance induced by screening effects from excess reagent exposure and over-production of byproducts in a temporal state was examined. Four inlet configurations were designed, discretized into finite elements, and later simulated through computational fluid dynamics (CFD) software to study the spatiotemporal behavior of the gases and examine the times required to achieve complete wafer exposure to reagents and minimize the residence time of gases through cut-in purging and output geometry modification. Results indicated that the combined ring-shaped and round-shaped inlet plate as well as four outflow ports were sufficient to achieve all the aforementioned objectives. This geometry can then be integrated into a multiscale CFD model to evaluate the discrete feed method approach on the surface coverage of the wafer.

CRediT authorship contribution statement

Matthew Tom: Conceptualization, Methodology, Software, Manuscript writing. **Henrik Wang:** Conceptualization, Methodology, Software, Manuscript writing. **Feiyang Ou:** Conceptualization, Methodology, Software. **Sungil Yun:** Conceptualization, Methodology, Software. **Gerassimos Orkoulas:** Manuscript reviewing and editing. **Panagiotis D. Christofides:** Manuscript reviewing and editing.

Declaration of competing interest

The authors declare that they have no known competing financial interests or personal relationships that could have appeared to influence the work reported in this paper.

Data availability

Data will be made available on request.

Acknowledgments

Financial support from the National Science Foundation is gratefully acknowledged. This work used computational and storage services associated with the Hoffman2 Shared Cluster provided by UCLA Institute for Digital Research and Education's Research Technology Group.

References

Andreoni, W., Yip, S., 2020. Handbook of Materials Modeling: Methods: Theory and Modeling, second ed. Springer International Publishing, Cham.
Anitha, V.C., Banerjee, A.N., Joo, S.W., 2015. Recent developments in TiO_2 as n- and p-type transparent semiconductors: synthesis, modification, properties, and energy-related applications. J. Mater. Sci. 50, 7495–7536.
ANSYS, 2022a. Ansys Fluent Theory Guide. ANSYS Inc., Canonsburg, PA.
ANSYS, 2022b. Ansys Fluent User's Guide. ANSYS Inc., Canonsburg, PA.
Asenov, A., Wang, Y., Cheng, B., Wang, X., Asenov, P., Al-Ameri, T., Georgiev, V.P., 2016. Nanowire transistor solutions for 5nm and beyond. In: Proceedings of 17th International Symposium on Quality Electronic Design. Santa Clara, CA, USA, pp. 269–274.
Cao, K., Cai, J., Chen, R., 2020. Inherently selective atomic layer deposition and applications. Chem. Mater. 32, 2195–2207.
Carver, C.T., Plombon, J.J., Romero, P.E., Suri, S., Tronic, T.A., Jr., R.B.T., 2015. Atomic layer etching: An industry perspective. ECS J. Solid State Sci. Technol. 4, N5005.
Chandrasekar, A., Zhang, S., Mhaskar, P., 2023. A hybrid hubspace-RNN based approach for modelling of non-linear batch processes. Chem. Eng. Sci. 281, 119118.
Chen, R., Kim, H., McIntyre, P.C., Porter, D.W., Bent, S.F., 2005. Achieving area-selective atomic layer deposition on patterned substrates by selective surface modification. Appl. Phys. Lett. 86, 191910.
Chen, Y., Li, Z., Dai, Z., Yang, F., Wen, Y., Shan, B., Chen, R., 2023. Multiscale CFD modelling for conformal atomic layer deposition in high aspect ratio nanostructures. Chem. Eng. J. 472, 144944.
Christofides, P.D., Armaou, A., Lou, Y., Varshney, A., 2009. Control and Optimization of Multiscale Process Systems. Birkhäuser, Boston, MA.
Cong, W., Li, Z., Cao, K., Feng, G., Chen, R., 2020. Transient analysis and process optimization of the spatial atomic layer deposition using the dynamic mesh method. Chem. Eng. Sci. 217, 115513.
Dahmen, K.-H., 2003. Chemical vapor deposition. In: Meyers, R.A. (Ed.), Encyclopedia of Physical Science and Technology, third ed. Academic Press, New York, pp. 787–808.
De la Huerta, C.M., Nguyen, V.H., Dedulle, J.-M., Bellet, D., Jiménez, C., Muñoz-Rojas, D., 2018. Influence of the geometric parameters on the deposition mode in spatial atomic layer deposition: A novel approach to area-selective deposition. Coatings 9, 5.
Deng, Z., He, W., Duan, C., Chen, R., Shan, B., 2016a. Mechanistic modeling study on process optimization and precursor utilization with atmospheric spatial atomic layer deposition. J. Vac. Sci. Technol. A 34, 01A108.
Deng, Z., He, W., Duan, C., Shan, B., Chen, R., 2016b. Atomic layer deposition process optimization by computational fluid dynamics. Vacuum 123, 103–110.
Dziczek, K., 2022. Why the automotive chip crisis isn't over (yet). Chicago Fed Letter. 1–7.
Elers, K.-E., Blomberg, T., Peussa, M., Aitchison, B., Haukka, S., Marcus, S., 2006. Film uniformity in atomic layer deposition. Chem. Vapor Depos. 12, 13–24.
Faraz, T., Roozeboom, F., Knoops, H.C.M., Kessels, W.M.M., 2015. Atomic layer etching: What can we learn from atomic layer deposition? ECS J. Solid State Sci. Technol. 4, N5023–N5032.
George, S.M., 2010. Atomic layer deposition: An overview. Chem. Rev. 110, 111–131.
Handwerker, C., 2021. A global semiconductor shortage highlights a troubling trend: A small and shrinking number of the world's computer chips are made in the US. Conversation.
Holmqvist, A., Törndahl, T., Stenström, S., 2012. A model-based methodology for the analysis and design of atomic layer deposition processes-Part I: Mechanistic modelling of continuous flow reactors. Chem. Eng. Sci. 81, 260–272.
Huang, J., 2022. Research progresses on suppressing the short-channel effects of field-effect transistor. Highlights Sci. Eng. Technol. 27, 361–367.
Johnson, R.W., Hultqvist, A., Bent, S.F., 2014. A brief review of atomic layer deposition: from fundamentals to applications. Mater. Today 17, 236–246.
Kanarik, K.J., Lill, T., Hudson, E.A., Sriraman, S., Tan, S., Marks, J., Vahedi, V., Gottscho, R.A., 2015. Overview of atomic layer etching in the semiconductor industry. J. Vac. Sci. Technol. A 33, 020802.
Kimes, W.A., Moore, E.F., Maslar, J.E., 2012. Perpendicular-flow, single-wafer atomic layer deposition reactor chamber design for use with in situ diagnostics. Rev. Sci. Instrum. 83, 083106.
Lee, H.-B.-R., Bent, S.F., 2011. Nanopatterning by area-selective atomic layer deposition. In: Pinna, N., Knez, M. (Eds.), Atomic Layer Deposition of Nanostructured Materials. John Wiley & Sons, Weinheim, pp. 193–225.
Lee, C.-W., Cho, T.-L., Kim, M.-S., 2017. Is there a better semiconductor firm in Taiwan? Manage. Econ. Rev. 2, 37–46.
Lee, A.J., Lee, S., Han, D.H., Kim, Y., Jeon, W., 2023. Enhancing chemisorption efficiency and thin-film characteristics via a discrete feeding method in high-k dielectric atomic layer deposition for preventing interfacial layer formation. J. Mater. Chem. C 11, 6894–6901.

Lee, F., Marcus, S., Shero, E., Wilk, G., Swerts, J., Maes, J.W., Blomberg, T., Delabie, A., Gros-Jean, M., Deloffre, E., 2007. Atomic layer deposition: An enabling technology for microelectronic device manufacturing. In: Proceedings of IEEE/SEMI Advanced Semiconductor Manufacturing Conference. Stresa, Italy, pp. 359–365.

Li, J., Tezsevin, I., Merkx, M.J.M., Maas, J.F.W., Kessels, W.M.M., Sandoval, T.E., Mackus, A.J.M., 2022. Packing of inhibitor molecules during area-selective atomic layer deposition studied using random sequential adsorption simulations. J. Vac. Sci. Technol. A 40, 062409.

Lin, S.-C., Wang, C.-C., Tien, C.-L., Tung, F.-C., Wang, H.-F., Lai, S.-H., 2023. Fabrication of aluminum oxide thin-film devices based on atomic layer deposition and pulsed discrete feed method. Micromachines 14.

Loubet, N., Hook, T., Montanini, P., Yeung, C.-W., Kanakasabapathy, S., Guillom, M., Yamashita, T., Zhang, J., Miao, X., Wang, J., Young, A., Chao, R., Kang, M., Liu, Z., Fan, S., Hamieh, B., Sieg, S., Mignot, Y., Xu, W., Seo, S.-C., Yoo, J., Mochizuki, S., Sankarapandian, M., Kwon, O., Carr, A., Greene, A., Park, Y., Frougier, J., Galatage, R., Bao, R., Shearer, J., Conti, R., Song, H., Lee, D., Kong, D., Xu, Y., Arceo, A., Bi, Z., Xu, P., Muthinti, R., Li, J., Wong, R., Brown, D., Oldiges, P., Robison, R., Arnold, J., Felix, N., Skordas, S., Gaudiello, J., Standaert, T., Jagannathan, H., Corliss, D., Na, M.-H., Knorr, A., Wu, T., Gupta, D., Lian, S., Divakaruni, R., Gow, T., Labelle, C., Lee, S., Paruchuri, V., Bu, H., Khare, M., 2017. Stacked nanosheet gate-all-around transistor to enable scaling beyond finFET. In: Proceedings of Symposium on VLSI Technology. Kyoto, Japan, pp. T230–T231.

Mackus, A.J.M., Bol, A.A., Kessels, W.M.M., 2014. The use of atomic layer deposition in advanced nanopatterning. IEEE Electron Device Lett. 6, 10941–10960.

Mackus, A.J.M., Merkx, M.J.M., Kessels, W.M.M., 2019. From the bottom-up: Toward area-selective atomic layer deposition with high selectivity. Chem. Mater. 31, 2–12.

Mameli, A., Merkx, M.J.M., Karasulu, B., Roozeboom, F., Kessels, W.E.M.M., Mackus, A.J.M., 2017. Area-selective atomic layer deposition of SiO_2 using acetylacetone as a chemoselective inhibitor in an ABC-type cycle. ACS Nano 11, 9303–9311.

Maroudas, D., 2000. Multiscale modeling of hard materials: Challenges and opportunities for chemical engineering. AIChE J. 46, 878–882.

Meng, J., Goodrich, J., 2021. Global governments ramp up pace of chip investments. Semicond. Ind. Assoc..

Merkx, M.J.M., Angelidis, A., Mameli, A., Li, J., Lemaire, P.C., Sharma, K., Hausmann, D.M., Kessels, W.M.M., Sandoval, T.E., Mackus, A.J.M., 2022. Relation between reactive surface sites and precursor choice for area-selective atomic layer deposition using small molecule inhibitors. J. Phys. Chem. C 126, 4845–4853.

Merkx, M.J.M., Sandoval, T.E., Hausmann, D.M., Kessels, W.M.M., Mackus, A.J.M., 2020. Mechanism of precursor blocking by acetylacetone inhibitor molecules during area-selective atomic layer deposition of SiO_2. Chem. Mater. 32, 3335–3345.

Mohammad, W., Elomri, A., Kerbache, L., 2022. The global semiconductor chip shortage: Causes, implications, and potential remedies. IFAC-PapersOnLine 55 (10), 476–483.

Moore, G.E., 1998. Cramming more components onto integrated circuits. Proc. IEEE 86, 82–85.

Mousa, M.B.M., Oldham, C.J., Parsons, G.N., 2015. Precise nanoscale surface modification and coating of macroscale objects: Open-environment in loco atomic layer deposition on an automobile. ACS Appl. Mater. Interfaces 7, 19523–19529.

Muneshwar, T., Cadien, K., 2016. A_xBA_xB... pulsed atomic layer deposition: Numerical growth model and experiments. J. Appl. Phys. 119, 085306.

Muñoz-Rojas, D., Nguyen, V.H., De la Huerta, C.M., Jiménez, C., Bellet, D., 2019. Spatial atomic layer deposition. In: Mandracci, P. (Ed.), Chemical Vapor Deposition for Nanotechnology. IntechOpen, London, pp. 1–25.

Pan, D., 2021. Density functional theory (DFT)-enhanced computational fluid dynamics modeling of substrate movement and chemical deposition process in spatial atomic layer deposition. Chem. Eng. Sci. 234, 116447.

Pan, D., Jen, T.-C., Yuan, C., 2016. Effects of gap size, temperature and pumping pressure on the fluid dynamics and chemical kinetics of in-line spatial atomic layer deposition of Al_2O_3. Int. J. Heat Mass Transfer 96, 189–198.

Park, T.J., Kim, J.H., Jang, J.H., Kim, U.K., Lee, S.Y., Lee, J., Jung, H.S., Hwang, C.S., 2011. Improved growth and electrical properties of atomic-layer-deposited metal-oxide film by discrete feeding method of metal precursor. Chem. Mater. 23, 1654–1658.

Petti, L., Münzenrieder, N., Vogt, C., Faber, H., Büthe, L., Cantarella, G., Bottacchi, F., Anthopoulos, T.D., Tröster, G., 2016. Metal oxide semiconductor thin-film transistors for flexible electronics. Appl. Phys. Rev. 3, 021303.

Ponraj, J.S., Attolini, G., Bosi, M., 2013. Review on atomic layer deposition and applications of oxide thin films. Crit. Rev. Solid State Mater. Sci. 38, 203–233.

Poodt, P., Cameron, D.C., Dickey, E., George, S.M., Kuznetsov, V., Parsons, G.N., Roozeboom, F., Sundaram, G., Vermeer, A., 2012. Spatial atomic layer deposition: A route towards further industrialization of atomic layer deposition. J. Vac. Sci. Technol. A 30, 010802.

Powell, M., Glasse, C., Green, P., French, I., Stemp, I., 2000. An amorphous silicon thin-film transistor with fully self-aligned top gate structure. IEEE Electron Device Lett. 21, 104–106.

Puurunen, R.L., 2005. Surface chemistry of atomic layer deposition: A case study for the trimethylaluminum/water process. J. Appl. Phys. 97, 121301.

Rashid, M., Mhaskar, P., 2023. Are neural networks the right tool for process modeling and control of batch and batch-like processes? Processes 11, 686.

Ritala, M., Leskelä, M., 2002. Chapter 2 - Atomic layer deposition. In: Singh Nalwa, H. (Ed.), Handbook of Thin Films. Academic Press, Burlington, pp. 103–159.

Schram, T., Sutar, S., Radu, I., Asselberghs, I., 2022. Challenges of wafer-scale integration of 2D semiconductors for high-performance transistor circuits. Adv. Mater. 34, 2109796.

Siimon, H., Aarik, J., 1997. Thickness profiles of thin films caused by secondary reactions in flow-type atomic layer deposition reactors. J. Phys. D: Appl. Phys. 30, 1725–1728.

Swanson, A., 2023. The CHIPS act is about more than chips: Here's what's in it. N. Y. Times.

Tom, M., Yun, S., Wang, H., Ou, F., Orkoulas, G., Christofides, P.D., 2023. Multiscale modeling of spatial area-selective thermal atomic layer deposition. In: Kokossis, A.C., Georgiadis, M.C., Pistikopoulos, E. (Eds.), Proceedings of 33rd European Symposium on Computer Aided Process Engineering. In: Computer Aided Chemical Engineering, vol. 52, Athens, Greece, pp. 71–76.

Wang, S., Liu, X., Zhou, P., 2022. The road for 2D semiconductors in the silicon age. Adv. Mater. 34, 2106886.

Wang, H., Wang, Z., Xu, X., Liu, Y., Chen, C., Chen, P., Hu, W., Duan, Y., 2019. Multiple short pulse process for low-temperature atomic layer deposition and its transient steric hindrance. Appl. Phys. Lett. 114, 201902.

Xiong, S., Jia, X., Mi, K., Wang, Y., 2021. Upgrading polytetrafluoroethylene hollow-fiber membranes by CFD-optimized atomic layer deposition. J. Membr. Sci. 617, 118610.

Xu, W., Haeve, M.G.N., Lemaire, P.C., Sharma, K., Hausmann, D.M., Agarwal, S., 2022. Functionalization of the SiO_2 surface with aminosilanes to enable area-selective atomic layer deposition of Al_2O_3. Langmuir 38, 652–660.

Yarbrough, J., Pieck, F., Grigjanis, D., Oh, I.-K., Maue, P., Tonner-Zech, R., Bent, S.F., 2022. Tuning molecular inhibitors and aluminum precursors for the area-selective atomic layer deposition of Al_2O_3. Chem. Mater. 34, 4646–4659.

Yarbrough, J., Shearer, A.B., Bent, S.F., 2021. Next generation nanopatterning using small molecule inhibitors for area-selective atomic layer deposition. J. Vac. Sci. Technol. A 39, 021002.

Yun, S., Ou, F., Wang, H., Tom, M., Orkoulas, G., Christofides, P.D., 2022a. Atomistic-mesoscopic modeling of area-selective thermal atomic layer deposition. Chem. Eng. Res. Des. 188, 271–286.

Yun, S., Tom, M., Orkoulas, G., Christofides, P.D., 2022b. Multiscale computational fluid dynamics modeling of spatial thermal atomic layer etching. Comput. Chem. Eng. 163, 107861.

Yun, S., Tom, M., Ou, F., Orkoulas, G., Christofides, P.D., 2022c. Multiscale computational fluid dynamics modeling of thermal atomic layer etching: Application to chamber configuration design. Comput. Chem. Eng. 161, 107757.

Yun, S., Wang, H., Tom, M., Ou, F., Orkoulas, G., Christofides, P.D., 2023. Multiscale CFD modeling of area-selective atomic layer deposition: Application to reactor design and operating condition calculation. Coatings 13, 558.